

# Artificial neural network for myelin water imaging

Submitted to **Magnetic Resonance in Medicine**

Jieun Lee<sup>1</sup>, Doohee Lee<sup>1</sup>, Joon Yul Choi<sup>1,2</sup>, Dongmyung Shin<sup>1</sup>,  
Hyeong-Geol Shin<sup>1</sup>, and Jongho Lee<sup>1,\*</sup>

<sup>1</sup>Laboratory for Imaging Science and Technology, Department of Electrical and Computer Engineering,  
Seoul National University, Seoul, Republic of Korea

<sup>2</sup>Cleveland Clinic, Epilepsy Center, Neurological Institute, OH, USA

\*Corresponding author: Jongho Lee, Ph.D. (e-mail: jonghoyi@snu.ac.kr)

## Abstract

**Purpose:** To demonstrate the application of artificial-neural-network (ANN) for real-time processing of myelin water imaging (MWI).

**Methods:** Three neural networks, ANN-I<sub>MWF</sub>, ANN-I<sub>GMT<sub>2</sub></sub>, and ANN-II, were developed to generate MWI. ANN-I<sub>MWF</sub> and ANN-I<sub>GMT<sub>2</sub></sub> were designed to output myelin water fraction (MWF) and geometric mean T<sub>2</sub> (GMT<sub>2</sub>), respectively whereas ANN-II generates a T<sub>2</sub> distribution. For the networks, gradient and spin echo data from 18 healthy controls (HC) and 26 multiple sclerosis patients (MS) were utilized. Among them, 10 HC and 12 MS had the same scan parameters and were used for training (6 HC and 6 MS), validation (1 HC and 1 MS), and test sets (3 HC and 5 HC). The remaining data had different scan parameters and were applied to exam the effects of the scan parameters. The network results were compared with those of conventional MWI in the white matter mask and regions of interest (ROI).

**Results:** The networks produced highly accurate results, showing averaged normalized root-mean-squared error under 3% for MWF and 0.4% for GMT<sub>2</sub> in the white matter mask of the test set. In the ROI analysis, the differences between ANNs and conventional MWI were less than 0.1% in MWF and 0.1 ms in GMT<sub>2</sub> (no statistical difference and  $R^2 > 0.97$ ). Datasets with different scan parameters showed increased errors. The average processing time was 0.68 sec in ANNs, gaining 11,702 times acceleration in the computational speed (conventional MWI: 7,958 sec).

**Conclusion:** The proposed neural networks demonstrate the feasibility of real-time processing for MWI with high accuracy.

**Keywords:** Myelin water imaging, artificial neural network, T<sub>2</sub> distribution, multi-echo spin echo, multiple sclerosis, deep learning

## Introduction

Myelin water imaging (MWI) is an MRI technique that acquires a signal from water confined in the gap between myelin lipid bilayers (1). This signal, which is referred to as the myelin water signal, has distinguishably shorter  $T_2$  relaxation than those of axonal and extra-cellular water signals. As a result, one can generate a voxel-wise  $T_2$  distribution of the water compartments by measuring  $T_2$  decay (1). From this  $T_2$  distribution, quantitative metrics such as myelin water fraction, which is the ratio of myelin water signal to total water signal, and geometric mean  $T_2$  ( $GMT_2$ ), which is the geometric mean of long  $T_2$  signal, are extracted to explore the integrity of white matter (2-6). Unfortunately, data processing to generate the  $T_2$  distribution is computationally expensive when correcting for stimulated echoes (7). It often takes several hours for the processing of the whole brain data. As a result, this data processing is performed off-line, hampering the ability to ensure the quality of myelin water images during a scan session.

In recent years, artificial neural networks (ANN) have been proposed as a promising tool to process complex biomedical data (8). ANN is known to provide a good approximation for complex functions and is computationally efficient (9). Additionally, computation in ANN is commonly performed using a graphical processing unit (GPU), which massively parallelizes computation to boost efficiency. By taking these advantages, ANN has been applied for a number of data processing tasks including curve fitting (10,11) and inverse problems (12-15) and has demonstrated the ability to process large size data in substantially shorter processing time than that of conventional methods.

In this study, we took advantage of the computational efficiency of ANN to demonstrate the feasibility of generating whole brain MWI in less than a second. Three different networks, ANN- $I_{MWF}$ , ANN- $I_{GMT_2}$ , and ANN-II, were developed. ANN-I was designed to generate MWF (ANN- $I_{MWF}$ ) and  $GMT_2$  (ANN- $I_{GMT_2}$ ) maps directly from  $T_2$  decay data. On the other hand, ANN-II generated a voxel-wise  $T_2$  distribution from which MWF and  $GMT_2$  values were calculated.

Source codes for our ANNs are available at <https://github.com/snu-list/ANN-MWI>.

## Methods

### *MRI data*

MRI data from previously published studies (6,16) were used. The data were from 18 healthy controls (HC) (7 males and 11 females; mean age =  $35.7 \pm 7.2$  years) and 26 multiple sclerosis (MS) patients (11 males and 15 females; mean age =  $34.2 \pm 6.5$  years). The subjects were scanned at a 3T Trio MRI scanner (Siemens Healthcare, Erlangen, Germany) using a 32-channel phased array head coil under the approval of the institutional review board.

For MWI, a 3D multiple echo gradient and spin echo (GRASE) sequence, which was proposed for MWI (17), was utilized. The scan parameters were as follows: FOV =  $240 \times 180 \times 112$  mm<sup>3</sup>, voxel dimensions =  $1.5 \times 1.5 \times 4$  mm<sup>3</sup>, number of slices = 28, TR = 1000 ms, number of echoes = 32, echo-planar imaging factor = 3, flip angle =  $90^\circ$ , and acquisition time = 14 min 5 sec. The default scan parameters for the first echo time (TE<sub>1</sub>) and echo spacing were set to be 10 ms each and were used in 22 subjects (10 HC and 12 MS). For the other subjects (remaining 22 subjects), slightly longer TEs were used (TE<sub>1</sub> = 10.1 ms for 3 HC and 8 MS, and TE<sub>1</sub> = 10.2 ms for 5 HC and 6 MS) with longer TRs to meet a specific absorption rate limit.

Additionally, three clinical protocol scans were used to detect lesions: 2D T<sub>1</sub>-weighted spin echo imaging (in-plane resolution =  $0.8 \times 0.7$  mm<sup>2</sup>; slice thickness = 3.2 mm; number of slices = 32; TR = 550 ms; TE = 9.2 ms; and flip angle =  $70^\circ$ ), 2D T<sub>2</sub>-weighted fast spin echo imaging (in-plane resolution =  $0.5 \times 0.5$  mm<sup>2</sup>; slice thickness = 3.2 mm; number of slices = 32; TR = 8750 ms; echo train length = 21; TE = 90 ms; and echo spacing = 11.3 ms), and 2D FLAIR imaging (in-plane resolution =  $0.7 \times 0.7$  mm<sup>2</sup>; slice thickness = 3.2 mm; number of slices = 32; TR = 9000 ms; TE = 87 ms; TI = 2500 ms; echo train length = 16; and echo spacing = 8.74 ms).

### *Conventional MWI*

Using the multi-echo GRASE data, MWI was generated as a reference for ANNs. The data processing started with a Tukey window (coefficient = 0.33) applied to the k-space of the multi-echo images in order to suppress Gibb's artifacts. Then voxel-wise multi-echo data were processed to generate a T<sub>2</sub> distribution by fitting stimulated-echo corrected multi-exponential functions (7). The following parameters were used for the fitting: the number of exponential

functions = 120;  $T_2$  range = 15 to 2000 ms, logarithmically spaced; and chi-square regularization. From the  $T_2$  distribution, MWF was calculated by dividing the sum of the signals from 15 to 40 ms by the sum of the entire  $T_2$  distribution. Additionally, the geometric mean  $T_2$  of the main water peak between 40 ms and 200 ms was calculated using

$$\text{GMT}_2 = \exp \left[ \frac{\sum_{j=M_1}^{M_2} S(T_{2,j}) \log T_{2,j}}{\sum_{j=M_1}^{M_2} S(T_{2,j})} \right] \quad (1)$$

Where  $\text{GMT}_2$  is the geometric mean,  $S(T_{2,j})$  is the amplitude of the  $T_2$  distribution at  $T_{2,j}$ , and  $j = M_1$  and  $j = M_2$  correspond to  $T_2$  of 40 ms and 200 ms, respectively (18). This approach of generating MWI is referred to as conventional MWI hereafter.

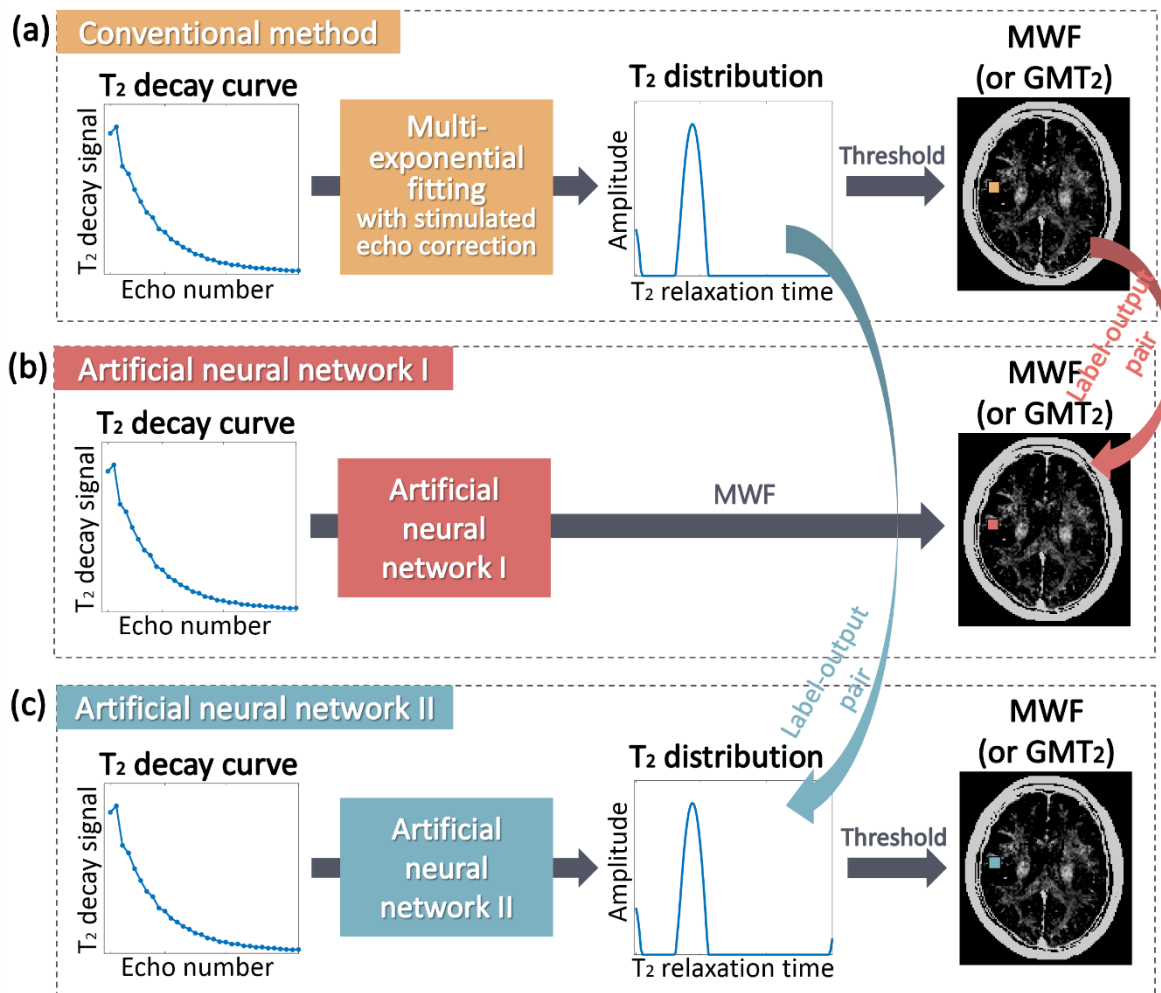


**Figure 1.** Conceptual illustration of the conventional MWI method (a), artificial neural network 1 (ANN- $I_{\text{MWF}}$  and ANN- $I_{\text{GMT}_2}$ ; b), and artificial neural network 2 (ANN-II; c). ANN-I was trained to generate MWF (ANN- $I_{\text{MWF}}$ ) or GMT<sub>2</sub> (ANN- $I_{\text{GMT}_2}$ ) from the  $T_2$  decay curve whereas ANN-II was trained to generate the  $T_2$  distribution.

## *Artificial neural networks for MWI*

In this work, three different artificial neural networks, ANN-I<sub>MWF</sub>, ANN-I<sub>GMT<sub>2</sub></sub>, and ANN-II, were developed (Fig. 1).

ANN-I was designed to generate MWF (ANN-I<sub>MWF</sub>) or GMT<sub>2</sub> (ANN-I<sub>GMT<sub>2</sub></sub>) directly from T<sub>2</sub> decay data by training the network with the 32-echo GRASE data of a voxel as an input and the MWF or GMT<sub>2</sub> from the conventional MWI as a label (Fig. 1b). The networks for MWF and GMT<sub>2</sub> were trained separately, generating ANN-I<sub>MWF</sub> and ANN-I<sub>GMT<sub>2</sub></sub>. The networks had 32 neurons in the input layer and one neuron in the output layer. Between the input and output layers, seven hidden layers were constructed with 160, 240, 320, 360, 480, 520, and 600 fully connected neurons. A leaky rectified linear unit ( $\alpha = 0.2$ ) was used as a non-linear activation function (19). We utilized Adam optimizer (20) with a varying learning rate, which started from 0.001 and reduced by one-tenth at every predetermined epoch (900, 1200, 1500, and 1800 epochs) in order to enhance the training speed with more accurate generalization (21). The batch size was increased by one for each epoch from 2 to 2,002. This approach has shown to decrease the number of parameter updates and improve generalization and training performance (22). The loss function was defined as the mean squared error between the network output and the label data.

ANN-II was designed to generate a T<sub>2</sub> distribution by training the network with the 32-echo data of a voxel as an input and the T<sub>2</sub> distribution from the conventional MWI as a label (Fig. 1c). The network had the same structure as ANN-I except for the output layer, which had 120 neurons to represent the coefficients of the 120 exponential basis functions. The loss function was defined as the mean squared error between the network output and the T<sub>2</sub> distribution from the conventional MWI. The other hyper-parameters were the same as ANN-I. To enforce the non-negative nature of the T<sub>2</sub> distribution, the negative values in the output were forced to zero.

For all networks, the input and output training data were normalized to improve training accuracy and learning speed (23). For the input, the 32-echo data were divided by the first echo. In ANN-I<sub>MWF</sub> and ANN-I<sub>GMT<sub>2</sub></sub>, the GMT<sub>2</sub> values were divided by 100 while keeping the MWF values the same. For the output of ANN-II, the T<sub>2</sub> distribution was scaled to have the sum of the T<sub>2</sub> distribution to be 15 (see Discussion).

During network performance optimization, various data combinations were tested using the 22 subject datasets of the default scan parameters (10 HC and 12 MS; see Supplementary

Information). Finally, out of the 22 datasets, twelve datasets (6 HC and 6 MS) were used as a network training set, eight datasets (3 HC and 5 MS) were reserved as a test set, and two datasets (1 HC and 1 MS) were utilized as a validation set. The remaining datasets of the different scan parameters (22 subjects;  $TE_1 = 10.1$  ms for 3 HC and 8 MS; and  $TE_1 = 10.2$  ms for 5 HC and 6 MS) were utilized to test the effects of the scan parameters on network performance.

When training and testing the networks, two different masks, a brain mask and a white matter mask, were applied. The brain mask excluded voxels outside the brain and was used for the network training. It was created from the FLAIR image by extracting the brain (24) and transforming the result into an MWF map space (25). The white matter mask was generated using the  $T_1$ -weighted image over the  $T_2$ -weighted image as described in the work of Choi et al. (6). The mask was refined to exclude voxels with unrealistic MWF ( $MWF \geq 30\%$  or  $MWF = 0$ ). This white matter mask was utilized to evaluate an MWF map. The normalized root-mean-square error (NRMSE) was calculated in the white matter mask for the eight test subjects (both HC and MS) with the conventional MWI as a reference. Both MWF and  $GMT_2$  were compared. The total number of voxels for the network training and testing were approximately 1,400,000 and 430,000, respectively.

For quantitative comparison, the analysis was performed for the white matter mask and five regions of interest (ROIs): forceps minor, genu of the corpus callosum, posterior limb of the internal capsule (PLIC), splenium of the corpus callosum, and forceps major. The five ROIs were manually segmented guided by a reference (26). The three HCs in the test set were used for this analysis. A Wilcoxon signed-rank test was performed between the conventional MWF (or  $GMT_2$ ) and ANN MWF (or  $GMT_2$ ) maps for each ROI. Additionally, the voxel-wise correlation was calculated between the conventional MWF (or  $GMT_2$ ) and ANN MWF (or  $GMT_2$ ) for each ROI. Finally, a Bland-Altman plot was plotted for the five ROIs to analyze the agreement of MWF (or  $GMT_2$ ).

For MS patients, MWF and  $GMT_2$  were compared in the lesions of the five MS test set. A whole brain MS lesion ROI was generated by applying a threshold to the FLAIR image (6). Then, a Wilcoxon signed-rank test and the voxel-wise correlation between the conventional MWI and ANNs were performed for the lesion ROI. Additionally, the NRMSE was calculated in the MS lesion ROI.

ANN-II generates a voxel-wise  $T_2$  distribution and, therefore, is flexible in choosing a threshold for myelin water. To test the reliability of ANN-II for different thresholds, MWF

maps were generated with three different thresholds (30, 40, and 50 ms). The NRMSE was calculated for each threshold using the eight test set.

The network training and test were performed on a GPU workstation (NVIDIA GeForce GTX 1080 Ti GPU with Intel® Xeon(R) CPU E5-2603 v4 at 1.70 GHz) using TensorFlow (27). The conventional MWI was processed using the four CPU cores of the same workstation and MATLAB R2017b (Mathworks, Inc., Natick, MA). The processing time for the test (or inference) was compared for all methods by repeating the test ten times and averaging the processing time.

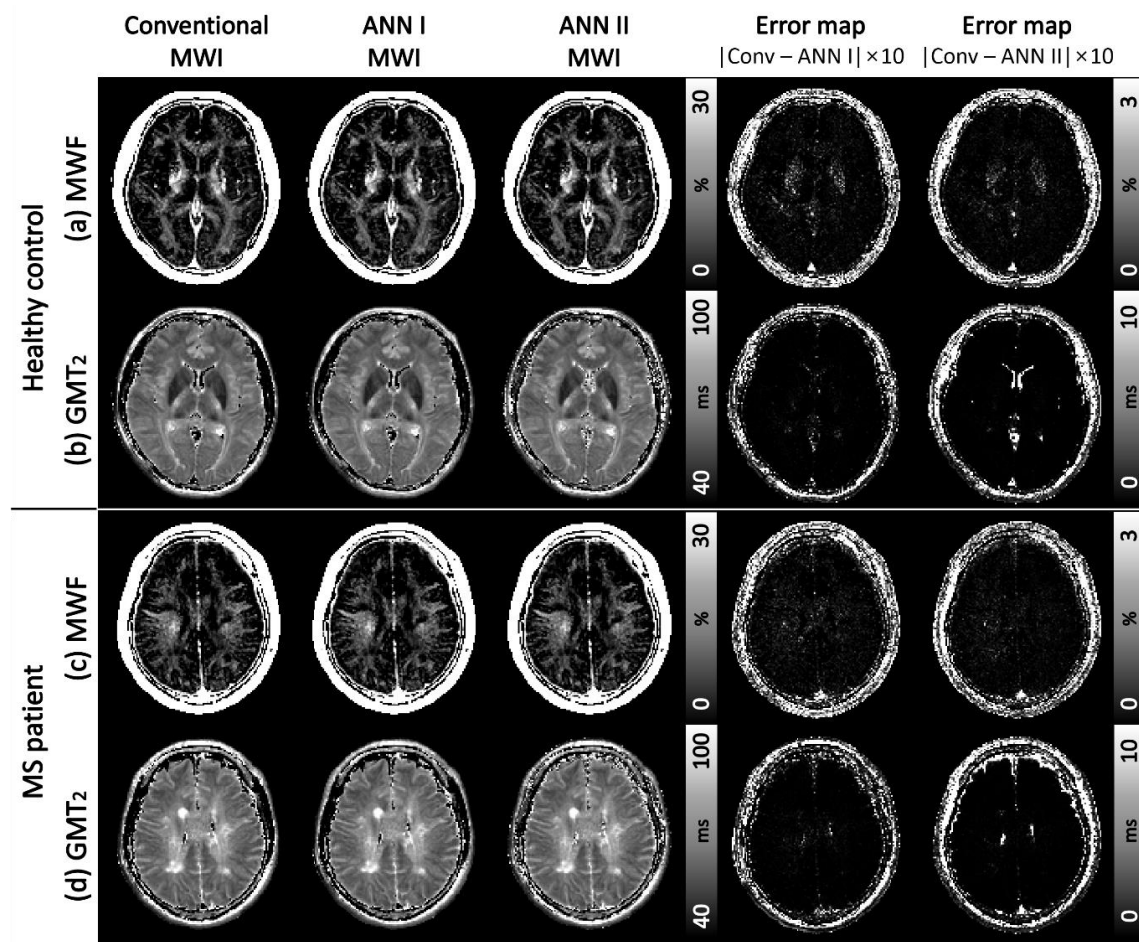


**Figure 2.** Myelin water fraction maps (a and c) and geometric mean T<sub>2</sub> maps (b and d) in a healthy control (upper rows) and an MS patient (lower rows) using the conventional MWI, ANN-I, and ANN-II. Error maps are displayed in 10 times smaller ranges.

## Results

The MWF and GMT<sub>2</sub> maps from the conventional MWI, ANN-I, and ANN-II are shown in Figure 2 for representative HC and MS. Additionally, the error maps, which are the absolute difference between the results of the conventional MWI and ANN MWI, are displayed in 10 times smaller ranges. The MWF and GMT<sub>2</sub> maps illustrate no visible difference among the three methods. This is also confirmed by the error maps, which reveal noticeable errors only outside of white matter. When the NRMSE is calculated in the white matter mask of the eight test set (both HC and MS), the average errors of MWF are  $2.86 \pm 0.29\%$  in ANN-I<sub>MWF</sub> (HC:  $3.01 \pm 0.03\%$ , MS:  $2.77 \pm 0.35\%$ ), and  $2.26 \pm 0.20\%$  in ANN-II (HC:  $2.33 \pm 0.06\%$ , MS:  $2.21 \pm 0.24\%$ ). The average NRMSEs of GMT<sub>2</sub> are  $0.34 \pm 0.03\%$  in ANN-I<sub>GMT<sub>2</sub></sub> (HC:  $0.34 \pm 0.04\%$ , MS:  $0.34 \pm 0.04\%$ ), and  $0.22 \pm 0.05\%$  in ANN-II (HC:  $0.18 \pm 0.02\%$ , MS:  $0.24 \pm 0.06\%$ ).

The results of the ROI analysis in the three HC test set are summarized in Table 1. The mean MWF and GMT<sub>2</sub> in the six ROIs, the white matter mask and five ROIs, reveal almost identical results in all methods. No statistically significant difference is observed in MWF and GMT<sub>2</sub>. Additionally, extremely high correlation values ( $R^2 > 0.99$ ) are reported for the voxel-wise correlation between the results of the ANNs and the conventional method in all ROIs. The Bland-Altman plots are included in Supplementary Figures S1 and S2, consolidating the results. A few examples of T<sub>2</sub> distributions from the conventional MWI and ANN-II are displayed in Figure S3. Each plot corresponds to a single pixel in the five ROIs (Figure S4). The results reconfirm the robust performance of ANN-II in generating voxel-wise T<sub>2</sub> distributions.

When the analysis is performed for the MS lesion ROI in the five MS test set, the same trends are observed in all metrics (Table 2). The mean NRMSEs of MWF in the lesion ROI are  $4.92 \pm 0.88\%$  in ANN-I<sub>MWF</sub>, and  $4.59 \pm 0.87\%$  in ANN-II, whereas those of GMT<sub>2</sub> are  $0.63 \pm 0.15\%$  in ANN-I<sub>GMT<sub>2</sub></sub>, and  $0.58 \pm 0.13\%$  in ANN-II. These results are higher than those from the white matter mask (see Discussion).



Healthy controls (n = 3)	Whole white matter	Forceps minor	Forceps major	Genu	Splenium	PLIC
(a) Conventional MWF (%)	7.4 ± 0.3	7.5 ± 0.9	11.5 ± 2.3	12.3 ± 2.7	15.2 ± 1.5	18.3 ± 1.3
(b) ANN-I MWF (%)	7.4 ± 0.3	7.5 ± 0.9	11.5 ± 2.3	12.2 ± 2.8	15.2 ± 1.4	18.3 ± 1.3
(c) ANN-II MWF (%)	7.4 ± 0.3	7.5 ± 0.9	11.5 ± 2.3	12.3 ± 2.7	15.2 ± 1.5	18.3 ± 1.3
<b>R<sup>2</sup> correlation between (a) and (b)</b>	0.99	0.99	0.99	0.99	0.99	0.99
<b>R<sup>2</sup> correlation between (a) and (c)</b>	0.99	0.99	0.99	0.99	0.99	0.99
(d) Conventional GMT <sub>2</sub> (ms)	63.2 ± 1.3	59.9 ± 2.3	72.6 ± 4.0	58.3 ± 3.8	67.3 ± 3.9	72.7 ± 4.5
(e) ANN-I GMT <sub>2</sub> (ms)	63.2 ± 1.3	59.9 ± 2.3	72.6 ± 4.0	58.3 ± 3.8	67.3 ± 3.9	72.7 ± 4.4
(f) ANN-II GMT <sub>2</sub> (ms)	63.2 ± 1.3	59.9 ± 2.3	72.6 ± 4.0	58.3 ± 3.8	67.3 ± 3.9	72.7 ± 4.5
<b>R<sup>2</sup> correlation between (d) and (e)</b>	1.00	0.99	0.99	0.99	0.99	0.99
<b>R<sup>2</sup> correlation between (d) and (f)</b>	1.00	1.00	1.00	1.00	1.00	0.99

**Table 1.** ROI analysis results in healthy controls. Mean ± standard deviation of MWF (%) and GMT<sub>2</sub> (ms) are reported in the white matter mask and five ROIs. When comparing the results of the conventional MWI and ANN-I or ANN-II, strong voxel-wise correlations ( $R^2 > 0.99$ ) are reported in all ROIs. PLIC represents the posterior limb of the internal capsule.

MS patients (n = 5)	Patient 1 lesion	Patient 2 lesion	Patient 3 lesion	Patient 4 lesion	Patient 5 lesion
(a) Conventional MWF (%)	6.7 ± 4.3	6.8 ± 5.2	3.9 ± 2.6	5.2 ± 3.3	3.1 ± 4.3
(b) ANN-I MWF (%)	6.7 ± 4.3	6.8 ± 5.2	3.9 ± 2.6	5.2 ± 3.3	3.1 ± 4.3
(c) ANN-II MWF (%)	6.6 ± 4.3	6.8 ± 5.2	3.9 ± 2.6	5.2 ± 3.3	3.1 ± 4.3
<b>R<sup>2</sup> correlation between (a) and (b)</b>	0.99	0.99	0.98	0.99	0.99
<b>R<sup>2</sup> correlation between (a) and (c)</b>	0.99	0.99	0.98	0.99	0.99
(d) Conventional GMT <sub>2</sub> (ms)	98.7 ± 19.6	84.2 ± 13.8	96.8 ± 15.5	91.0 ± 16.9	91.8 ± 12.6
(e) ANN-I GMT <sub>2</sub> (ms)	98.6 ± 19.5	84.2 ± 13.8	96.7 ± 15.5	91.1 ± 16.9	91.7 ± 12.6
(f) ANN-II GMT <sub>2</sub> (ms)	98.7 ± 19.1	84.2 ± 13.8	96.7 ± 15.5	91.0 ± 16.8	91.7 ± 12.5
<b>R<sup>2</sup> correlation between (d) and (e)</b>	0.99	0.99	0.99	0.99	0.99
<b>R<sup>2</sup> correlation between (d) and (f)</b>	0.97	0.99	0.99	0.99	0.99

**Table 2.** ROI analysis results in MS patients. Mean ± standard deviation of MWF (%) and GMT<sub>2</sub> (ms) are reported in the MS lesions. When comparing the results of the conventional MWI and ANN-I or ANN-II, strong voxel-wise correlations ( $R^2 > 0.97$ ) are reported in all ROIs.

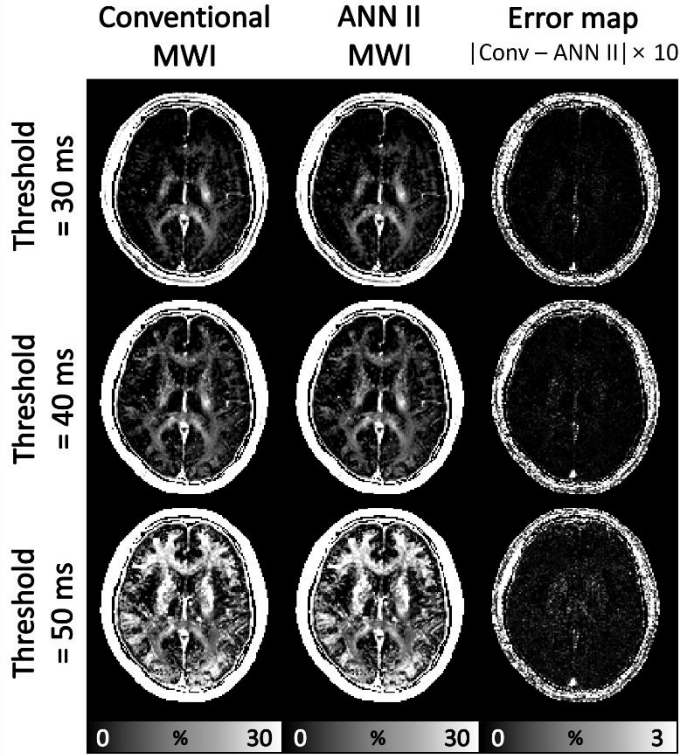


**Figure 3.** MWF maps from the three different thresholds (30, 40, and 50 ms) with error maps displayed in a ten times smaller range. The MWF maps show similar contrasts in all cases, demonstrating the robustness of ANN-II in generating the  $T_2$  distribution.

Figure 3 shows the MWF maps from the three different myelin water thresholds (30, 40, and 50 ms), demonstrating the flexibility and robustness of ANN-II in generating MWF maps with the different thresholds. The mean NRMSEs in the white matter mask of the eight test data are  $2.65 \pm 0.34\%$ ,  $2.26 \pm 0.20\%$ , and  $2.27 \pm 0.19\%$  for the thresholds of 30, 40, and 50 ms, respectively.

When the datasets with different TEs are applied to the network, they result in increased errors of MWI when compared to the datasets with TE = 10 ms. For the datasets with TE = 10.1 ms, the NRMSEs of MWI are  $4.32 \pm 0.48\%$  in ANN-I<sub>MWF</sub> (HC:  $4.24 \pm 0.18\%$ , MS:  $4.35 \pm 0.56\%$ ), and  $4.02 \pm 0.56\%$  in ANN-II (HC:  $4.05 \pm 0.13\%$ , MS:  $4.01 \pm 0.67\%$ ). For TE = 10.2 ms datasets, the NRMSEs of MWI are  $8.02 \pm 0.84\%$  in ANN-I<sub>MWF</sub> (HC:  $8.00 \pm 0.58\%$ , MS:  $8.04 \pm 1.07\%$ ), and  $7.90 \pm 0.83\%$  in ANN-II (HC:  $7.92 \pm 0.55\%$ , MS:  $7.88 \pm 1.07\%$ ).

When the processing times of the whole brain data are compared, the ANN methods (0.68 sec) are approximately 11,702 times faster than the conventional method (7,958 sec or 2.2 hours), demonstrating the feasibility of applying the neural networks for real-time processing of MWI.

## Discussion

In this study, we developed fast and robust data processing approaches for MWI by using ANN. The results showed under 3% of average NRMSE in MWF and 0.4% in GMT<sub>2</sub> while gaining 11,702 times faster computational speed (less than 1 sec for ANNs vs. over 2.2 hours for conventional MWI).

As summarized in Tables 1 and 2, the maximum difference in the ROI-averaged MWF was less than 0.1% (0.06%) when comparing the conventional MWI and ANNs. No statistically significant difference was reported in all ROIs. The same results were observed for the GMT<sub>2</sub> results, revealing the maximum difference of less than 0.1 ms (0.09 ms). These results suggest that ANNs may be applied for an ROI analysis with high reliability.

Although the inference of the ANNs can be performed almost in real time, the network training took approximately 12 hours in our single GPU workstation. This training is required once and, therefore, does not hamper the real-time processing of new data.

In this work, the processing speeds of the ANNs and the conventional MWI were compared using the processors that were optimized for each processing (i.e., one GPU for the ANNs and quad-core CPU for the conventional MWI). When the comparison was performed using the same processor (one CPU core) for all methods, the ANNs took 25.2 sec whereas the conventional MWI took 28,250 sec. In this case, the computational speed of the ANNs was 1121 times faster than that of the conventional MWI, confirming computational efficiency of the ANNs.

During the development of the networks, optimization was performed for the training of different subject types (Supplementary Figure S5) and different numbers of subjects (Supplementary Figure S6). When the effects of the subject type were explored using three different compositions of training sets (6 HC only; 6 MS only; 3 HC and 3 MS combined) for three ROIs (white matter in HC; white matter in MS excluding MS lesions; MS lesions), the networks that included MS patients for training showed less errors in the MS lesions (Supplementary Figure S5). When the effect of the training data size was investigated by increasing the training data size from 2 to 12 subjects with an equal number of HC and MS, the NRMSE showed the best results at 12 subjects (Supplementary Figure S6). These two optimization results led us to train the networks using the 12 subjects (6 HC and 6 MS).

In our results, larger NRMSEs were observed in the MS lesions when compared to those from the white matter mask of the test set. This performance degradation may be explained by

an imbalanced number of voxels between the lesion and non-lesion white matter since the MS lesions were approximately 0.3% of the total number of data (28). Further reduction in the NRMSE may be achieved by balancing training data between non-lesion and lesion by oversampling lesion data (29).

When normalizing the data for the networks, the multi-echo GRASE data of each voxel was divided by the first echo signal in order to set the range of the data approximately from 0 to 1 (23). A logical approach for data normalization is to set the signal at TE of 0 ms being equal to the sum of the  $T_2$  distribution. However, the  $T_2$  distribution is not available for inference data and, therefore, multi-echo data cannot be normalized using the distribution. As an alternative option, we set the first echo to 1.

In our results, the data with different TEs showed increased errors, suggesting the dependency of the ANNs on TE and echo spacing. This outcome may be explained by  $T_2$  decay variations for the different TE and echo spacing. To reduce the errors, one may train a network for each TE at the cost of increased training datasets. When training different TE datasets, transfer learning can be used to reduce the size of training datasets (30).

The ANNs may be applied for the diagnosis of other diseases such as neuromyelitis optica (31), schizophrenia (32), and phenylketonuria (33). However, further tests may be necessary to confirm the reliability of the results because errors may increase for untrained lesion types that have different  $T_2$  relaxation characteristics. If error increases, one may fine-tune the network with a few datasets using a transfer learning method (30) to improve the performance.

## **Conclusions**

In this work, we proposed three different neural networks for the real-time processing of MWI. The accuracy of the networks in estimating MWF and  $GMT_2$  was close to the results of the conventional MWI. The gain in the computational speed was almost 10,000 times. The proposed networks were capable of estimating not only MWF and  $GMT_2$  (both ANN-I and ANN-II) but also  $T_2$  distribution (ANN-II), and were applicable to healthy controls and MS patients. Our results demonstrated the potentials of applying a neural network for myelin water imaging.

## **Acknowledgment**

This work was supported by the National Research Foundation of Korea grant funded by the Korea government (NRF-2018R1A2B3008445) and Creative-Pioneering Researchers Program through Seoul National University. The Institute of Engineering Research at Seoul National University provided research facilities for this work.

This work is an extension of a previously published ISMRM abstract of the same authors (34).

## References

1. Mackay A, Whittall K, Adler J, Li D, Paty D, Graeb D. In vivo visualization of myelin water in brain by magnetic resonance. *Magnetic resonance in medicine* 1994;31(6):673-677.
2. Kolind S, Matthews L, Johansen-Berg H, Leite MI, Williams SC, Deoni S, Palace J. Myelin water imaging reflects clinical variability in multiple sclerosis. *Neuroimage* 2012;60(1):263-270.
3. Levesque IR, Giacomini PS, Narayanan S, Ribeiro LT, Sled JG, Arnold DL, Pike GB. Quantitative magnetization transfer and myelin water imaging of the evolution of acute multiple sclerosis lesions. *Magnetic resonance in medicine* 2010;63(3):633-640.
4. Vavasour IM, Whittall KP, Mackay AL, Li DK, Vorobeychik G, Paty DW. A comparison between magnetization transfer ratios and myelin water percentages in normals and multiple sclerosis patients. *Magnetic resonance in medicine* 1998;40(5):763-768.
5. Laule C, Vavasour IM, Kolind SH, Traboulsee AL, Moore G, Li DK, MacKay AL. Long T<sub>2</sub> water in multiple sclerosis: What else can we learn from multi-echo T<sub>2</sub> relaxation? *Journal of Neurology* 2007;254(11):1579-1587.
6. Choi JY, Jeong IH, Oh SH, Oh CH, Park NY, Kim HJ, Lee J. Evaluation of Normal-Apparent White Matter in Multiple Sclerosis Using Direct Visualization of Short Transverse Relaxation Time Component (ViSTa) Myelin Water Imaging and Gradient Echo and Spin Echo (GRASE) Myelin Water Imaging. *Journal of Magnetic Resonance Imaging* 2019;49(4):1091-1098.
7. Prasloski T, Mädler B, Xiang QS, MacKay A, Jones C. Applications of stimulated echo correction to multicomponent T<sub>2</sub> analysis. *Magnetic resonance in medicine* 2012;67(6):1803-1814.
8. Schmidhuber J. Deep learning in neural networks: An overview. *Neural networks* 2015;61:85-117.
9. Hornik K, Stinchcombe M, White H. Multilayer feedforward networks are universal approximators. *Neural networks* 1989;2(5):359-366.
10. Lee D, Jung W, Ko J, Shin HG, Eun H, Nam Y, Lee J. SafeNet: Artificial Neural Network for Real-Time T<sub>2</sub> mapping with Quality Assurance. In: *Proceedings of the 26th Annual Meeting of International Society for Magnetic Resonance in Medicine*. Paris, France 2018. Abstract 2277.
11. Cohen O, Zhu B, Rosen MS. MR fingerprinting deep reconstruction network (DRONE). *Magnetic resonance in medicine* 2018;80(3):885-894.
12. Yoon J, Gong E, Chatnuntawech I, Bilgic B, Lee J, Jung W, Ko J, Jung H, Setsompop K, Zaharchuk G. Quantitative susceptibility mapping using deep neural network: QSMnet. *NeuroImage* 2018;179:199-206.
13. Hammernik K, Klatzer T, Kobler E, Recht MP, Sodickson DK, Pock T, Knoll F. Learning a variational network for reconstruction of accelerated MRI data. *Magnetic resonance in medicine* 2018;79(6):3055-3071.
14. Kang E, Min J, Ye JC. A deep convolutional neural network using directional wavelets for low-dose X-ray CT reconstruction. *Medical physics* 2017;44(10):e360-e375.
15. Jin KH, McCann MT, Froustey E, Unser M. Deep convolutional neural network for inverse problems in imaging. *IEEE Transactions on Image Processing* 2017;26(9):4509-4522.

16. Jeong I, Choi J, Kim SH, Hyun JW, Joung A, Lee J, Kim H. Normal-appearing white matter demyelination in neuromyelitis optica spectrum disorder. *European journal of neurology* 2017;24(4):652-658.
17. Prasloski T, Rauscher A, MacKay AL, Hodgson M, Vavasour IM, Laule C, Mädler B. Rapid whole cerebrum myelin water imaging using a 3D GRASE sequence. *Neuroimage* 2012;63(1):533-539.
18. Whittall KP, Mackay AL, Graeb DA, Nugent RA, Li DK, Paty DW. In vivo measurement of T<sub>2</sub> distributions and water contents in normal human brain. *Magnetic resonance in medicine* 1997;37(1):34-43.
19. Maas AL, Hannun AY, Ng AY. Rectifier nonlinearities improve neural network acoustic models. 2013. p 3.
20. Kingma DP, Ba J. Adam: A method for stochastic optimization. arXiv preprint arXiv:14126980 2014.
21. Wilson DR, Martinez TR. The need for small learning rates on large problems. 2001. IEEE. p 115-119.
22. Smith SL, Kindermans P-J, Ying C, Le QV. Don't decay the learning rate, increase the batch size. arXiv preprint arXiv:171100489 2017.
23. Sola J, Sevilla J. Importance of input data normalization for the application of neural networks to complex industrial problems. *IEEE Transactions on nuclear science* 1997;44(3):1464-1468.
24. Smith SM. Fast robust automated brain extraction. *Human brain mapping* 2002;17(3):143-155.
25. Smith SM, Jenkinson M, Woolrich MW, Beckmann CF, Behrens TE, Johansen-Berg H, Bannister PR, De Luca M, Drobnjak I, Flitney DE. Advances in functional and structural MR image analysis and implementation as FSL. *Neuroimage* 2004;23:S208-S219.
26. Shin H-G, Oh S-H, Fukunaga M, Nam Y, Lee D, Jung W, Jo M, Ji S, Choi JY, Lee J. Advances in gradient echo myelin water imaging at 3T and 7T. *NeuroImage* 2018.
27. Abadi M, Barham P, Chen J, Chen Z, Davis A, Dean J, Devin M, Ghemawat S, Irving G, Isard M. Tensorflow: A system for large-scale machine learning. 2016. p 265-283.
28. He H, Garcia EA. Learning from imbalanced data. *IEEE Transactions on Knowledge & Data Engineering* 2008(9):1263-1284.
29. Krawczyk B. Learning from imbalanced data: open challenges and future directions. *Prog Artif Intell* 2016;5(4):221-232.
30. Pan SJ, Yang QA. A Survey on Transfer Learning. *Ieee T Knowl Data En* 2010;22(10):1345-1359.
31. Jeong IH, Choi JY, Kim SH, Hyun JW, Joung A, Lee J, Kim HJ. Comparison of myelin water fraction values in periventricular white matter lesions between multiple sclerosis and neuromyelitis optica spectrum disorder. *Mult Scler* 2016;22(12):1616-1620.
32. Flynn SW, Lang DJ, Mackay AL, Gohari V, Vavasour IM, Whittall KP, Smith GN, Arango V, Mann JJ, Dwork AJ, Falkai P, Honer WG. Abnormalities of myelination in schizophrenia detected in vivo with MRI, and post-mortem with analysis of oligodendrocyte proteins. *Mol Psychiatry* 2003;8(9):811-820.
33. Sirrs SM, Laule C, Madler B, Brief EE, Tahir SA, Bishop C, MacKay AL. Normal-appearing white matter in patients with phenylketonuria: water content, myelin water fraction, and metabolite concentrations. *Radiology* 2007;242(1):236-243.
34. Lee J, Lee D, Choi JY, Shin D, Shin HG, Lee J. Real-time processing of myelin water imaging using artificial neural network. In: *Proceedings of the 27th Annual Meeting*

of International Society for Magnetic Resonance in Medicine. Montreal, Canada  
2019. Abstract 0425.